TOPOLOGICAL DERIVATIVE MULTISCALE APPROACH FOR THE DESIGN OF BROADBAND EPSILON-NEAR-ZERO METAMATERIALS

A.A. NOVOTNY, F.A. PINHEIRO AND P.J. BLANCO

Abstract. We put forward a novel application of the topological derivative method, in the context of multiscale electromagnetic material modeling, to the design of epsilon-near-zero (ENZ) metamaterials. Unlike conventional homogenization techniques, the proposed approach is valid for a broad frequency range and benefits from a well-defined variational structure. Leveraging this structure, we derive the sensitivity of the effective macroscopic electric permittivity tensor to microscale topological changes. By predicting unique ENZ plasmonic composites at a desired broad range of visible and near-infrared wavelengths, we demonstrate that the topological derivative approach allows for a systematic design of optimized ENZ metamaterials with nontrivial, unprecedented geometries responsible for functionalities that cannot be achieved with traditional metamaterial synthesis techniques.

1. Introduction

The generation, manipulation, and detection of light are key functionalities in photonics that rely on light–matter interactions in a crucial way. According to Maxwell's equations, these interactions are governed by two fundamental material parameters: the relative electric permittivity (ε_r) and relative magnetic permeability (μ_r), which together define the relative refractive index ($n_r = \sqrt{\varepsilon_r \mu_r}$).

Naturally occurring materials offer limited possibilities and degrees of freedom to control the refractive index contrast and its dispersion in time and frequency domains. Circumventing these limitations has driven notable progress in the field of metamaterials and photonics over the last years, allowing for unprecedented control over the spatiotemporal $(r,t) \in \mathbb{R}^3 \times \mathbb{R}^+$ engineering of $\varepsilon_r(r,t)$, $\mu_r(r,t)$, and consequently $n_r(r,t)$. Key advances in this field include the development of photonic crystals, based on periodic modulation of the refractive index [1]; plasmonic systems, which exploit materials exhibiting both positive and negative permittivity [2]; and negative-index metamaterials, which have demonstrated negative refractive indices [3]. Altogether, these innovations have substantially broadened the accessible parameter space for engineering light–matter interactions, leading to more precise control over electromagnetic wave propagation in material media, and paving the way for new functionalities and applications in photonics.

In the specific case of negative-index metamaterials, recent advances in nanofabrication techniques have enabled their operation at terahertz and visible frequencies. However, despite this progress, the negative refractive index response remains typically confined to narrow spectral bands. As a result, the refractive index ranges between positive and negative values, resulting in intermediate-frequency regions where it approaches zero. Such near-zero-index behavior can arise through three distinct scenarios, namely: epsilon-near-zero (ENZ), where $\varepsilon \to 0$; mu-near-zero (MNZ), where $\mu \to 0$; and epsilon-and-mu-near-zero (EMNZ), where both ε and μ simultaneously approach zero [4, 5, 6, 7]. These scenarios are central to the emerging field of near-zero-index (NZI) materials for photonics [4, 5,

---

Date: November 4, 2025.

Key words and phrases. Synthesis of electromagnetic media, ENZ metamaterial, topological derivative method.

6, 7, 8]. In the following, we focus exclusively on the design of epsilon-near-zero (ENZ) metamaterials.

ENZ materials exhibit a wide range of remarkable electromagnetic properties [9, 10, 11] such as perfect absorption [12], enhanced optical nonlinearities [13, 14, 15], and optimized coupling between waveguides that facilitates the development of integrated photonic devices [16]. Many of these unique electromagnetic properties are at the origin of a wide range of ENZ-based applications that include efficient geometry-independent antennas [17], terahertz wave generators [18], invisibility cloaks [19], and optomechanical devices [20]. There exist two major material platforms to design and engineer ENZ materials, namely naturally occuring materials and manmade, artificial metamaterials. Examples of the former class of materials include metals, semiconductors, oxides, and halides, which exhibit an intrinsic dielectric permittivity near zero [21]. In contrast, the latter class includes materials such as superlattices [22], multilayers [23], plasmonic systems [24], all-dielectric structured materials [25] and ENZ organic compounds [26]. In both classes of materials ENZ frequency bands are narrow, which not only hamper many applications but also motivate the development of alternative strategies for efficient design of optimized ENZ metamaterials. Therefore, to enable practical applications across various spectral ranges, it is essential to tune the frequency at which the ENZ condition occurs.

Beyond well-established topology optimization methods, such as SIMP [27], level-set [28], and phase-field approaches [29], in this paper we propose a novel topological derivative-based strategy for the synthesis of artificial metamaterials. The topological derivative method [30] enables a systematic design of physical systems, which naturally allows both shape and topology changes in the structure. In fact, the topological derivative method has been successfully applied in many different fields, including the synthesis of elastic microstructures by considering first [31] as well as second-order homogenized elasticity tensor [32]. See also further developments in [33, 34, 35, 36]. In the context of electromagnetism, a novel multiscale constitutive model for micro-structured electromagnetic media has been recently proposed in [37]. In contrast to conventional homogenization approaches, such a model is based on the Method of Multiscale Virtual Power applied to Maxwell's equations, so that its applicability ranges from low-frequency to high-frequency regimes. Since the model presents a clear variational structure, its sensitivity with respect to microscopic topological changes is derived here with the help of the topological derivative method. In particular, the resulting sensitivity leads to a second-order tensor field over the microstructure that measures how the effective macroscopic electric permittivity tensor estimated within the multiscale framework from [37] changes when a small topological perturbation is introduced at the microscale. The obtained result is used to devise a topology design algorithm for electromagnetic microstructures, which is applied in the context of the synthesis of epsilon-near-zero (ENZ) metamaterials. We demonstrate that the proposed method allows for the design of structures that are optimized to exhibit ENZ behavior at desired frequency domains, which should enable optimized functionalities at target wavelengths.

The paper is organized as follows. The adopted multiscale formalism used to estimate the effective electric permittivity is introduced in Section 2. The topological derivative of the effective electric permittivity with respect to topological microscopic changes is presented in Section 3. The resulting topology design algorithm, based on the topological gradient and a level-set domain representation method, is explained in detail in Section 4. A numerical experiment dealing with the synthesis of ENZ metamaterials for varying wavelengths is reported in Section 5. Some concluding remarks are highlighted in Section 6. Finally, the proof of the main result, summarized in Theorem 2, is outlined in all details in Section 7.

2. Multiscale Modeling

Let us consider a micro-structured electromagnetic material composed of cells periodically arranged. Each cell is represented by $\Omega \subset \mathbb{R}^3$, whose boundary is denoted by $\partial\Omega$. Following the original ideas by Blanco et al. [37], the effective permittivity is defined by the following second-order tensor written in terms of its Cartesian components

$$[\varepsilon_{\text{eff}}]_{ij} = \frac{1}{|\Omega|}\int_\Omega n^2\left(\delta_{ij} + [E^{(j)}]_i\right) dx, \quad \text{with} \quad i,j = 1,2,3. \tag{2.1}$$

where δ_{ij} is the Kronecker delta and n is the refractive index of the cell medium. Each $E^{(j)} : \Omega \mapsto \mathbb{C}^3$, for $j = 1,2,3$, is solution to the cell-problem of the form: Find $E^{(j)} \in \mathcal{V}$, such that

$$\int_\Omega \left(\nabla \times E^{(j)} \cdot \nabla \times W - k_0^2 n^2 E^{(j)} \cdot W\right) dx = \int_\Omega k_0^2 n^2 e_j \cdot W dx \quad \forall W \in \mathcal{V}, \tag{2.2}$$

where $e_j \in \mathbb{R}^3$ is the jth-canonical Cartesian direction and k_0 is the wave-number. The space $\mathcal{V}$ is defined as follows:

$$\mathcal{V} := \{V \in H_{\text{curl}}(\Omega;\mathbb{C}^3) : \langle V\rangle = 0, \text{with } V \ \partial\Omega\text{-periodic}\}, \tag{2.3}$$

where $H_{\text{curl}}(\Omega;\mathbb{C}^3)$ is used to denote the standard complex-valued Hilbert space of vector functions $V : \Omega \mapsto \mathbb{C}^3$, such that $V \in L^2(\Omega;\mathbb{C}^3)$ and $\nabla \times V \in L^2(\Omega;\mathbb{C}^3)$. In addition,

$$\langle(\cdot)\rangle := \int_\Omega (\cdot)\, dx. \tag{2.4}$$

Finally, we assume that the refractive index at the microcell n is given by a piece-wise constant function of the form

$$n = n_1 \quad \text{in} \quad \Omega_1 \qquad \text{and} \qquad n = n_2 \quad \text{in} \quad \Omega_2, \tag{2.5}$$

with $\Omega = \Omega_1 \cup \Omega_2$, such that $\Omega_1 \cap \Omega_2 = \varnothing$. Therefore, we can define the contrast $\gamma = \gamma(x)$ on the material property as follows

$$\gamma = \frac{n_2}{n_1} \quad \text{in} \quad \Omega_1 \qquad \text{and} \qquad \gamma = \frac{n_1}{n_2} \quad \text{in} \quad \Omega_2. \tag{2.6}$$

Definition 1. *In the case of isotropic constitutive response, the effective electric permittivity from* (2.1) *can be written as* $[\varepsilon_{\text{eff}}]_{ij} = \varepsilon\, \delta_{ij}$*, where* δ_{ij} *is the Kronecker delta and* $\varepsilon \in \mathbb{C}$*. Let us denote the effective refractive index as* $n_{\text{eff}} = \sqrt{\varepsilon}$*, with* $n_{\text{eff}} = n'_{\text{eff}} + \mathbf{i}n''_{\text{eff}}$*, where* n'_{eff} *and* n''_{eff} *are the real and imaginary parts of* n_{eff}*, with* $\mathbf{i} = \sqrt{-1}$*. The so-called ENZ property is attained when* $\varepsilon' \approx 0$*, which implies* $n'_{\text{eff}} \approx n''_{\text{eff}}$*.*

3. Topological Derivative Method

The topological derivative is a relatively new concept originally designed to deal with topology optimization [38, 39]. It is defined as the first term of the asymptotic expansion of a given shape functional with respect to a small parameter that measures the size of singular domain perturbations, such as holes, inclusions, source-terms and cracks. This concept can naturally be used as the steepest descent direction in an optimization process, like any method based on the gradient of a cost functional. Therefore, the topological derivative method has been successfully applied in many different fields such as image processing, inverse problems, multi-scale material design, and mechanical modeling, including damage and fracture evolution phenomena. For a comprehensive overview of the most recent developments on the topological derivative method, the reader may refer to the collection of articles in the special issue *On the topological derivative and its applications in computational engineering* [40], for instance. In this paper, we are interested in the optimal design of electromagnetic media. Therefore, we derive the sensitivity of the effective electric permittivity with respect to the nucleation of a spherical inclusion at the microscopic level. This result can be summarized as follows.

Theorem 2. *The topological derivative of the effective permittivity second-order tensor* ε_{eff} *with respect to the nucleation of a small spherical inclusion, endowed with a different material property from the background, is given, for* $i, j = 1, 2, 3$, *by*

$$[D_T\varepsilon_{\text{eff}}]_{ij}(x) = -\frac{1-\gamma^2}{|\Omega|} n^2 (\delta_{ij} + [E^{(i)}]_j + [E^{(j)}]_i + E^{(i)} \cdot E^{(j)})(x) \quad \forall x \in \Omega, \tag{3.1}$$

where n *is the refractive index of the microcell domain* (2.5), γ *is the contrast* (2.6) *and* $E^{(k)}$ *are the electric vector fields, solutions to the cell-problems* (2.2) *for* $k = 1, 2, 3$.

Proof. The proof of this result is given in Section 7. □

The expression (3.1) allows us to calculate the *exact* topological derivative of any differentiable function of ε_{eff} by direct application of the conventional rules of differential calculus. That is, any such function $\psi : \mathbb{C}^3 \times \mathbb{C}^3 \mapsto \mathbb{C}$ has exact topological derivative of the form

$$D_T\psi = \langle D\psi(\varepsilon_{\text{eff}}), D_T\varepsilon_{\text{eff}} \rangle \ , \tag{3.2}$$

with the brackets $\langle \cdot, \cdot \rangle$ denoting the appropriate product between the derivative $D\psi(\varepsilon_{\text{eff}})$ of ψ with respect to ε_{eff} and the topological derivative of ε_{eff}, called $D_T\varepsilon_{\text{eff}}$. This observation points strongly to the suitability of the use of (3.2) in a topology algorithm for the synthesis and optimal design of electromagnetic micro-structured metamaterials based on the minimization/maximization of cost functions defined in terms of effective properties.

4. TOPOLOGY DESIGN ALGORITHM

Following the original ideas introduced by Amstutz & Andrä [41], in this section, we present a topology design algorithm based on the topological derivative of a shape functional $J : \Omega \mapsto \mathbb{R}$ combined with a level-set domain representation method for solving the optimization problem we are dealing with. In particular, the domains Ω_1 and Ω_2 are characterized by a level-set function $\Psi : \Omega \mapsto \mathbb{R}$ of the form

$$\Omega_1 = \{x \in \Omega : \Psi(x) < 0\} \qquad \text{and} \qquad \Omega_2 = \{x \in \Omega : \Psi(x) > 0\}. \tag{4.1}$$

We define the steepest descent direction $g : \Omega \mapsto \mathbb{R}$ as follows

$$g(x) := \begin{cases} -D_T J(x), & \text{if } \Psi(x) < 0, \\ +D_T J(x), & \text{if } \Psi(x) > 0, \end{cases} \tag{4.2}$$

which will be referred to as *topological gradient* of the shape functional $J(\Omega)$. For future reference, we also define a gradient $G : \Omega \mapsto \mathbb{C}^3 \times \mathbb{C}^3$ of the form:

$$G(x) := \begin{cases} -D_T\varepsilon_{\text{eff}}(x), & \text{if } \Psi(x) < 0, \\ +D_T\varepsilon_{\text{eff}}(x), & \text{if } \Psi(x) > 0. \end{cases} \tag{4.3}$$

The components of tensor G are given by

$$G_{ij}(x) = -\frac{n_2^2 - n_1^2}{|\Omega|} (\delta_{ij} + [E^{(i)}]_j + [E^{(j)}]_i + E^{(i)} \cdot E^{(j)})(x), \tag{4.4}$$

where we have used (4.3) and (3.1), together with the definition for the contrast (2.6). Finally, the angle θ between the level-set function Ψ and the descent direction g is given by

$$\theta = \arccos \left[\frac{\langle g, \Psi \rangle_{L^2(\Omega)}}{\|g\|_{L^2(\Omega)} \|\Psi\|_{L^2(\Omega)}} \right], \tag{4.5}$$

so that $\theta = 0$ represents a local optimality condition, which has been rigorously derived in [42].

From these elements, a topology optimization algorithm can be devised. In particular, for a generic iteration $j \in \mathbb{N}$, the updated level-set function is governed by the following equation derived in [41, Section 3.2] with the help of Euler's scheme on a sphere and trigonometric formulas:

$$\Psi_{j+1} = \frac{1}{\sin\theta_j}\left[\sin((1-k)\theta_j)\Psi_j + \sin(k\theta_j)\frac{g_j}{\|g_j\|_{L^2(\Omega)}}\right], \tag{4.6}$$

where k is a step size determined by a line-search procedure to decrease the value of the shape functional. The algorithm is initialized by setting $\Psi_0 = -1$ or $\Psi_0 = 1$ for the whole optimization region or any spatial distribution of these two values. The process ends when the condition $\theta_j < \epsilon_\theta$ is satisfied at some iteration j, where ϵ_θ is a given small numerical tolerance. If k is found to be smaller than a given numerical tolerance ϵ_k and the local optimality condition is not yet satisfied, namely $\theta_j > \epsilon_\theta$, then a mesh refinement of the domain is carried out to increase the set of possible local minima. At this stage, the level-set defined in the coarse mesh is mapped to the new refined mesh using standard interpolation of the element shape functions, and the process is continued. The material properties n_1 or n_2 are assigned to elements of the mesh depending on whether they are at points with $\Psi_j(x) < 0$ or $\Psi_j(x) > 0$. The elements eventually crossed by the phase interface (defined by $\Psi_j(x) = 0$) will have value n_1 by choice. Obviously, according to the above procedure, the solution of the optimal material distribution depends directly on the refinement of the adopted mesh. The overall optimization procedure is conveniently summarized in pseudo-code format through Algorithm 1.

5. SYNTHESIS OF ENZ METAMATERIALS

We consider the problem of finding a microstructure that produces an effective permittivity close to zero. It is known as the epsilon-near-zero (ENZ) property [43], in which the real part of ε_{eff} vanishes. The choice of the shape functional $J : \Omega \mapsto \mathbb{R}$ that may induce such a behavior is crucial and probably not unique. It is important to stress that there is no axiomatic procedure to define the shape functional, so it depends strongly on the intuition over the problem we are dealing with.

5.1. **Shape Functional.**

For the synthesis of ENZ electromagnetic metamaterials, we define the following shape functional to be minimized:

$$J(\Omega) = \alpha J_1(\Omega) + (1-\alpha)J_2(\Omega), \tag{5.1}$$

with $\alpha \in [0,1]$ and

$$J_1(\Omega) = [\varepsilon'_{\text{eff}}]_{ii}^2 \quad \text{and} \quad J_2(\Omega) = \left([\varepsilon'_{\text{eff}}]_{ii} + |[\varepsilon_{\text{eff}}]_{ii}| - [\varepsilon''_{\text{eff}}]_{ii}\right)^2, \tag{5.2}$$

where we use the Einstein summation convention over the repeated index i, with $i = 1, 2, 3$. The motivation for such a choice emerges from Definition 1. Actually, $J_1(\Omega)$ is precisely the real part of $[\varepsilon_{\text{eff}}]_{ii}$ squared. On the other hand, $J_2(\Omega)$ is related to $([n'_{\text{eff}}]_{ii} - [n''_{\text{eff}}]_{ii})^2$, where $[n_{\text{eff}}]_{ii} := \sqrt{[\varepsilon_{\text{eff}}]_{ii}}$. Therefore, minimizing $J(\Omega)$ means to minimize $[\varepsilon'_{\text{eff}}]_{ii}^2$ and the misfit between $[n'_{\text{eff}}]_{ii}$ and $[n''_{\text{eff}}]_{ii}$, for a given weight α.

5.2. **Topological Gradient.**

From Theorem 2, the topological gradient (4.2) of $J(\Omega)$ is given by the sum

$$g(x) = \alpha g_1(x) + (1-\alpha)g_2(x), \tag{5.3}$$

Algorithm 1: The topology design algorithm

```
   Input: $\Omega$, $\Psi_0, \epsilon_k, \epsilon_\theta$
   Output: $\Omega^\star$
1  begin
2      $j \leftarrow 0$; $\Omega_j \leftarrow \Psi_j$;
3      compute the shape functional $J(\varepsilon_{\text{eff}})$;
4      compute the topological derivative $D_T J$;
5      compute the steepest descent direction $g$ and angle $\theta$;
6      $\Psi_{old} \leftarrow \Psi_j$; $J_{old} \leftarrow J(\varepsilon_{\text{eff}})$; $J_{new} \leftarrow 1 + J_{old}$; $k \leftarrow 1$; $\theta_{old} \leftarrow \theta$;
7      while $J_{new} > J_{old}$ do
8          compute $\Psi_{new}$ according to (4.6);
9          $\Psi_j \leftarrow \Psi_{new}$;
10         execute line 3;
11         $J_{new} \leftarrow J(\varepsilon_{\text{eff}})$;
12         $k \leftarrow k/2$;
13     end
14     if $k < \epsilon_k$ then
15         refine the mesh;
16         $\Psi_{j+1} \leftarrow \Psi_j$; $j \leftarrow j + 1$;
17         go to line 3;
18     else
19         if $\theta > \epsilon_\theta$ then
20             $\Psi_{j+1} \leftarrow \Psi_j$; $j \leftarrow j + 1$;
21             go to line 3;
22         else
23             return $\Omega^\star \leftarrow \Psi_j$;
24         end
25     end
26 end
```

where

$$g_1(x) = 2[\varepsilon'_{\text{eff}}]_{ii} G'_{ii}(x) \quad \text{and} \tag{5.4}$$

$$g_2(x) = 2K_{ii}[G'_{ii} - G''_{ii} + |[\varepsilon_{\text{eff}}]_{ii}|^{-1}([\varepsilon'_{\text{eff}}]_{ii} G'_{ii} + [\varepsilon''_{\text{eff}}]_{ii} G''_{ii})](x), \tag{5.5}$$

with $K_{ii} := [\varepsilon'_{\text{eff}}]_{ii} - [\varepsilon''_{\text{eff}}]_{ii} + |[\varepsilon_{\text{eff}}]_{ii}|$, where, again, we use the Einstein summation convention over repeated indices.

5.3. **Numerical Results.** Given the topological gradient (5.3) of the shape functional (5.1), applied within Algorithm 1, we are in a position to design microstructures that enjoy ENZ behavior at the macroscopic level.

We consider a cube-shaped cell of dimensions $\ell \times \ell \times \ell$, with $\ell = 1000$ nm. The working wavelength is denoted by λ. The related wavenumber is computed as $k_0 = 2\pi/\lambda$. The refractive index of the medium n depends on the wavelength λ and is given in [44]. We consider the cell composed by either ITO+Ag or SIO2+Ag. For the reader convenience, the corresponding refractive indices n depending on λ to be used in this section are given in Table 1, extracted from Ref. [44].

Table 1. Refractive indices n depending on the wavelength λ.

λ	Ag	ITO	SIO2
400.0	0.050000 + 2.1035i	2.043800 + 0.0113550i	1.4701
450.0	0.040000 + 2.6484i	1.968800 + 0.0075303i	1.4656
500.0	0.050000 + 3.1309i	1.906900 + 0.0072965i	1.4623
550.0	0.059582 + 3.5974i	1.850400 + 0.0086145i	1.4599
600.0	0.055159 + 4.0097i	1.795400 + 0.0108980i	1.4580
650.0	0.052225 + 4.4094i	1.739500 + 0.0139820i	1.4565
700.0	0.041000 + 4.8025i	1.681200 + 0.0178870i	1.4553
750.0	0.031165 + 5.1949i	1.619200 + 0.0227330i	1.4542
800.0	0.036759 + 5.5698i	1.552600 + 0.0287000i	1.4533
850.0	0.040000 + 5.9655i	1.480200 + 0.0360560i	1.4525
900.0	0.040000 + 6.3711i	1.400900 + 0.0451750i	1.4518
950.0	0.040000 + 6.7407i	1.313400 + 0.0566330i	1.4511
1000.0	0.040000 + 7.1155i	1.215600 + 0.0713110i	1.4504
1050.0	0.040000 + 7.5016i	1.105000 + 0.0907570i	1.4498
1100.0	0.044688 + 7.8918i	0.977880 + 0.1178500i	1.4492
1150.0	0.064219 + 8.2954i	0.828330 + 0.1588800i	1.4486
1200.0	0.083750 + 8.6989i	0.649070 + 0.2302500i	1.4481
1250.0	0.097684 + 9.0723i	0.451790 + 0.3736100i	1.4475
1260.4	0.100030 + 9.1471i	0.415910 + 0.4160000i	1.4474
1300.0	0.108980 + 9.4317i	0.319590 + 0.5937800i	1.4469
1350.0	0.120280 + 9.7910i	0.264080 + 0.8041000i	1.4464
1400.0	0.130650 + 10.156i	0.240040 + 0.9859400i	1.4458
1450.0	0.135250 + 10.560i	0.229050 + 1.1471000i	1.4452
1500.0	0.139860 + 10.963i	0.224640 + 1.2939000i	1.4446
1688.7	0.171660 + 12.387i	0.233370 + 1.7719000i	1.4423

The basic idea consists in minimizing $J(\Omega)$ from (5.1) for varying wavelengths $\lambda^\star$. The initial guess is given by a spherical inclusion of n_1 material with radius $r = 200$ nm, surrounded by n_2 material. See Figure 1, where red and blue are n_1 and n_2 phases, respectively.

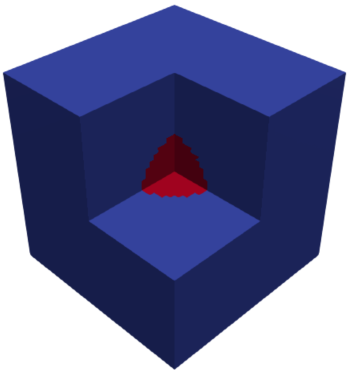

Figure 1. The initial guess is given by a cube-shaped cell with a spherical inclusion of n_1 material (red) surrounded by n_2 material (blue).

Finally, the variational equations (2.2) are approximated via the Finite Element Method by using Nédélec finite elements [45]. The topology design procedure summarized in Algorithm 1 is fully implemented by using FreeFEM++ library [46].

5.3.1. *Example 1: Cell composed by ITO+Ag.* Following Ref. [43], where Ag-ITO sputtered composite ENZ films have been experimentally synthesized in near-infrared, we chose an unit cell made of ITO and Ag, and a working wavelength λ ranging from 400 nm to 1500 nm. Note that ITO exhibits ENZ property in the neighborhood of $\lambda \approx 1260$ nm. The target wavelengths $\lambda^\star$ are given by 400, 600, 800 and 1000 nm. In all cases, the weight parameter α is set as 0.25, except for $\lambda^\star = 800$ nm, in which α is set as 0.9. Ag-ITO composite films have been shown to exhibit outstanding optical properties, particularly the tunability of their crossover wavelengths where the ENZ region occurs, which can be adjusted by modifying the silver content [43]. These unique optical properties cannot be achieved using Ag or ITO separately but, rather, results from the controlled balance of the proportion of either materials in the composite. Indeed, the introduction of Ag in the composite leads not only to a much stronger optical nonlinear response compared to a single ITO film but also the possibility of tuning ENZ frequency range and the plasmonic properties. However, the possibility of tuning optical properties in these Ag-ITO composites, in particular the ENZ behavior, by optimizing the composite geometry, has never been addressed so far. This is precisely our goal in the following to highlight the potential of topological derivative approach in optimizing the systhesis of ENZ metamaterials. It is worth mentioning that the geometry of composite inclusions is crucial for determining the effective optical properties of this class of materials [47].

The obtained real part of effective permittivities ε (normalized by the vacuum permittivity ε_0) as a function of the working wavelength λ are reported in Figure 2. First, the cell is not submitted to the optimization process and only the radius of the Ag inclusion varies from 100, 200, 300 up to 400 nm. The resulting effective permittivities are highlighted in cyan, showing ENZ behavior in between $1180 \sim 1330$ nm for a system not subjected to the optimization process, depending on the associated volume fraction v_f. Then, the cell is submitted to the optimization procedure according to Algorithm 1 for $\lambda^\star = 400$ nm (blue), $\lambda^\star = 600$ nm (red), $\lambda^\star = 800$ nm (magenta) and $\lambda^\star = 1000$ nm (green). Note that for the corresponding $\lambda^\star$, the resulting effective permittivity shows ENZ behavior. These points are indicated by $(*)$ in Figure 2. For the optimized topologies, we obtained broadband ENZ windows with wavelength spans of up to approximately 860 nm, covering the range from about 400 nm to 1260 nm. This ENZ bandwidth is significantly broader than previously reported values (≈ 300 nm) for ITO–Ag composite system [43], which served as the experimental reference for our numerical calculations. In addition, for $\lambda^\star = 600$ and $\lambda^\star = 1000$, ENZ frequency bands as large as 100 nm are also found. These bands are not observed in [43]. It is worth noting that, for $\lambda = 750$ nm, the effective permittivities are very close to each other in all cases ($\varepsilon \approx 3$). This phenomenon may explain why it was necessary to find a different weight α for $\lambda^\star = 800$ nm after several trials. Actually, finding the appropriate parameter α that minimizes $J(\Omega)$ for $\lambda^\star = 800$ nm was much more difficult than the other cases reported in Figure 2. Finally, the resulting optimal microstructures that produce the wavelength-specific ENZ property from Figure 2 are presented in Figures 3, 4, 5 and 6 for $\lambda^\star = 400$, $\lambda^\star = 600$, $\lambda^\star = 800$ and $\lambda^\star = 1000$ nm, respectively, where red and blue represent Ag and ITO phases. In all investigated cases, highly nontrivial, counterintuitive geometries for the unit cell were found, which have never been predicted so far using existing numerical methods.

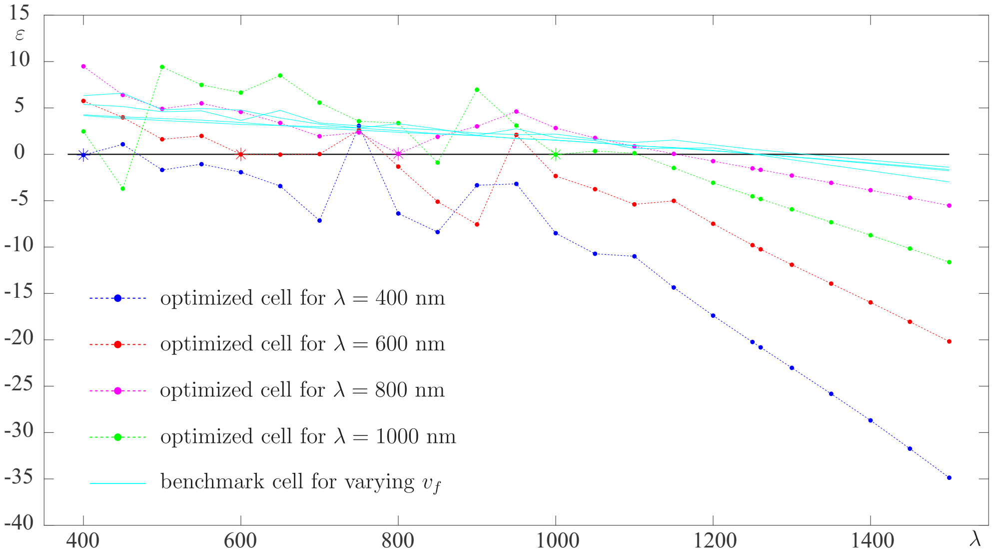

Figure 2. Obtained real part of the effective permittivities ε with respect to the working wavelength λ. The cube-shaped cell of ITO with a spherical inclusion of Ag of varying radius from 100, 200, 300 up to 400 nm shows ENZ behavior in between 1180$\sim$1330 nm (cyan) depending on the resulting volume fraction v_f. After the optimization procedure for $\lambda^\star = 400$ nm (blue), $\lambda^\star = 600$ nm (red), $\lambda^\star = 800$ nm (magenta) and $\lambda^\star = 1000$ nm (green), the resulting cells show ENZ behavior for each associated $\lambda^\star$, highlighted with ($*$). ENZ bands of about 100 nm for $\lambda^\star = 600$ nm (red) and $\lambda^\star = 1000$ nm (green) are worth of notice.

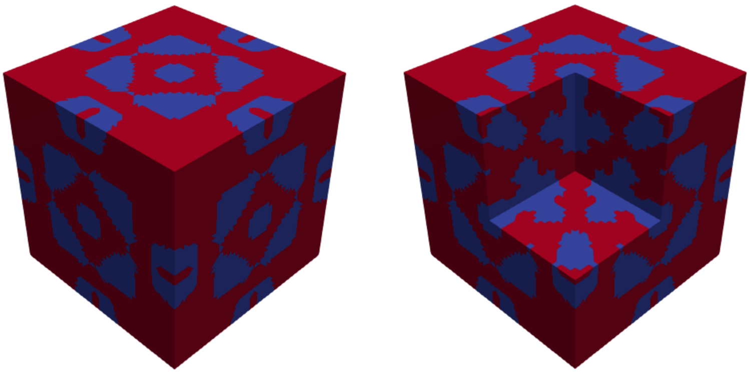

Figure 3. Optimal cell for $\lambda^\star = 400$ nm composed by ITO (blue) and Ag (red).

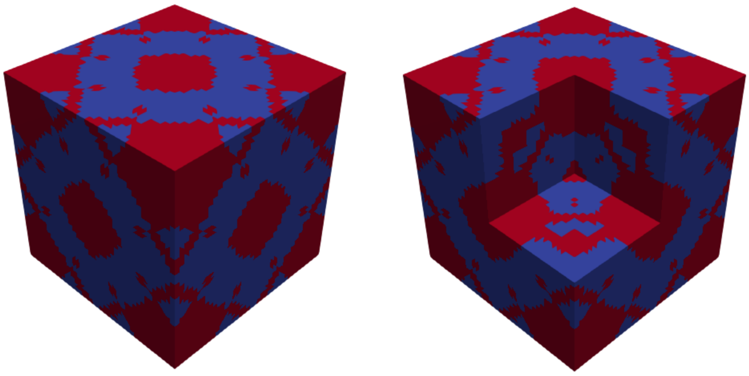

Figure 4. Optimal cell for $\lambda^\star = 600$ nm composed by ITO (blue) and Ag (red).

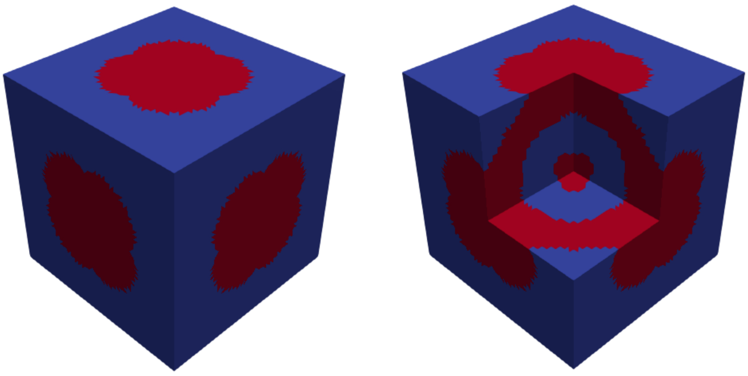

Figure 5. Optimal cell for $\lambda^\star = 800$ nm composed by ITO (blue) and Ag (red).

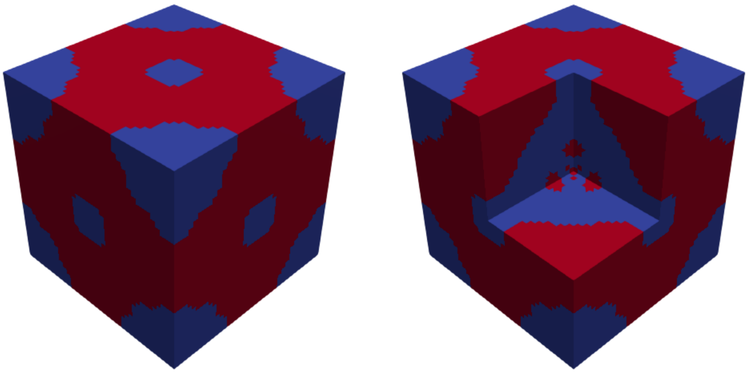

Figure 6. Optimal cell for $\lambda^\star = 1000$ nm composed by ITO (blue) and Ag (red).

5.3.2. *Example 2: Cell composed by SiO2+Ag.* Now, we consider the cell composed by SiO2 and Ag. The working wavelength λ ranges from 400 to 900 nm. Note that both SiO2 and Ag separately do not feature the ENZ property. The target wavelengths $\lambda^\star$ are given by 400 and 500 nm. In both cases, the weight parameter α is set to 1.0, so that only $J_1(\Omega)$ in expression (5.1) is minimized.

The obtained effective permittivities ε (normalized by ε_0) as a function of the working wavelength λ are reported in Figure 7. First, the cell is not submitted to the optimization process and only the radius of the Ag inclusion varies from 100, 200 up to 300 nm.

The resulting effective permittivities are highlighted in cyan, and no ENZ behavior occurs independently of the associated volume fraction v_f. Then, the cell is submitted to the optimization procedure according to Algorithm 1 for $\lambda^\star = 400$ nm (blue) and $\lambda^\star = 500$ nm (red). Again, for the corresponding $\lambda^\star$, we demonstrate that the resulting effective permittivity shows ENZ behavior. These points are highlighted with $(*)$ in Figure 7. In addition, ENZ bands of about $100 \sim 200$ nm are also found. Finally, the resulting optimal microstructures that produce the wavelength-specific ENZ property from Figure 7 are presented in Figures 8 and 9 for $\lambda^\star = 400$ nm and $\lambda^\star = 500$ nm, respectively, where red and blue represent Ag and SiO2 phases. As in the previous case, the topological derivative method predicts nontrivial ENZ structures that may guide nanofabrication process to design novel metamaterials.

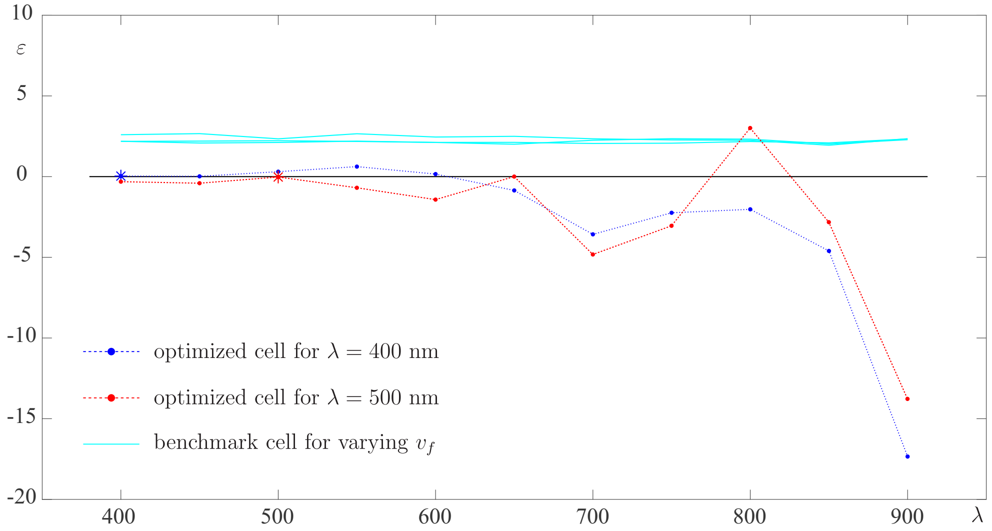

FIGURE 7. Obtained real part of the effective permittivities ε with respect to the working wavelength λ. The cube-shaped cell of SiO2 with a spherical inclusion of Ag of varying radius from 100, 200 up to 300 nm does not show ENZ behavior (cyan), regardless of the resulting volume fraction v_f. After the optimization procedure for $\lambda^\star = 400$ nm (blue) and $\lambda^\star = 500$ nm (red), the resulting cells enjoy ENZ behavior for each associated $\lambda^\star$, highlighted with $(*)$. ENZ bands are also found in both cases.

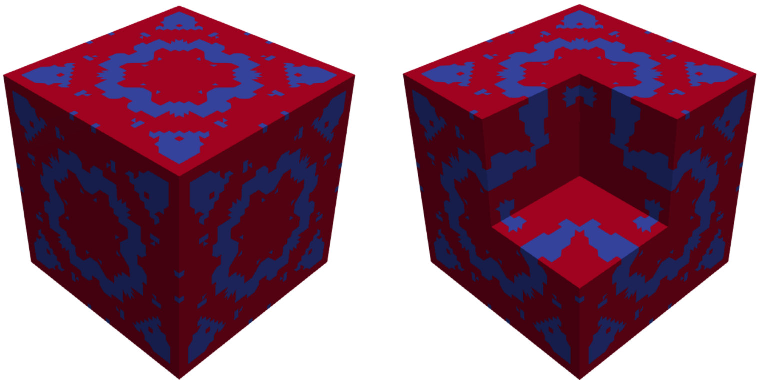

FIGURE 8. Optimal cell for $\lambda^\star = 400$ nm composed by SiO2 (blue) and Ag (red).

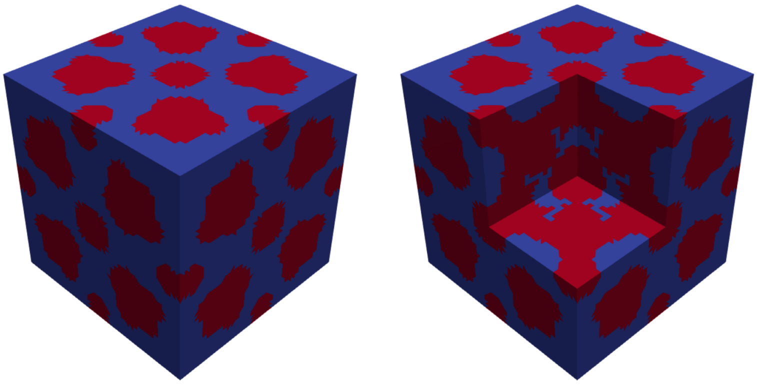

FIGURE 9. Optimal cell for $\lambda^\star = 500$ nm composed by SiO2 (blue) and Ag (red).

6. CONCLUSIONS

In summary, we introduced a novel multiscale design framework for epsilon-near-zero (ENZ) metamaterials using the topological derivative method. The adopted multiscale model offers a significant departure from traditional homogenization techniques by maintaining validity over a broad frequency range and relying on a rigorous variational foundation. Through the derivation of topological sensitivities of the effective macroscopic electric permittivity tensor, we unveil a direct and efficient connection between microscale structural modifications and target macroscopic electromagnetic responses that lead to ENZ behavior at desired visible and near-infrared frequencies. The resulting predicted structures, optimized ENZ plasmonic composites with nontrivial geometries, demonstrate the method's capability to reveal unique metamaterials beyond the reach of existing theoretical methods. These findings open new pathways for the systematic and scalable development of advanced ENZ metamaterials for broadband applications.

7. PROOF OF THE MAIN RESULT

Let us evaluate the topological derivative of ε_{eff} given by (2.1). From the definition for the contrast (2.6), we define the topologically perturbed counterpart of the problem by introducing a small inclusion $\mathcal{B}_\rho(\widehat{x})$, with center at $\widehat{x} \in \Omega$ and radius $\rho > 0$, endowed with different material property from the background. Thus we define

$$n_\rho = n \quad \text{in} \quad \Omega \setminus \mathcal{B}_\rho(\widehat{x}) \qquad \text{and} \qquad n_\rho = \gamma n \quad \text{in} \quad \mathcal{B}_\rho(\widehat{x}). \tag{7.1}$$

The perturbed counterpart of the j-th cell-problem reads: Find $E_\rho^{(j)} \in \mathcal{V}$, such that

$$\int_\Omega \left(\nabla \times E_\rho^{(j)} \cdot \nabla \times W - k_0^2 n_\rho^2 E_\rho^{(j)} \cdot W \right) dx = \int_\Omega k_0^2 n_\rho^2 e_j \cdot W dx \quad \forall W \in \mathcal{V}. \tag{7.2}$$

Thus, the perturbed effective second-order permittivity tensor $\varepsilon_{\text{eff}}^\rho$ is defined as follows

$$[\varepsilon_{\text{eff}}^\rho]_{ij} = \frac{1}{|\Omega|} \int_\Omega n_\rho^2 \left(\delta_{ij} + [E_\rho^{(j)}]_i \right) dx. \tag{7.3}$$

7.1. *A priori* estimate.

Lemma 3. *Let* $E^{(j)}$ *and* $E_\rho^{(j)}$ *be the solutions of the variational problems* (2.2) *and* (7.2), *respectively. Then, the following* a priori *estimate holds true:*

$$\|E_\rho^{(j)} - E^{(j)}\|_{\mathcal{V}} \leq C \rho^{\frac{3}{2}+\delta}, \tag{7.4}$$

with constant C *independent of the small parameter* ρ *and* $0 < \delta < 3/2$.

Proof. We start by rewriting (2.2) as follows:

$$\int_\Omega \left(\nabla\times E^{(j)}\cdot\nabla\times W - k_0^2 n_\rho^2 E^{(j)}\cdot W\right)dx = \int_\Omega k_0^2 n_\rho^2 e_j\cdot W dx \\ + \int_{\mathcal{B}_\rho}(1-\gamma^2)k_0^2 n^2 e_j\cdot W\,dx + \int_{\mathcal{B}_\rho}(1-\gamma^2)k_0^2 n^2 E^{(j)}\cdot W\,dx \quad \forall\, W\in\mathcal{V}, \tag{7.5}$$

where we have used the definition for the contrast (2.6). By subtracting (7.5) from (7.2) we obtain

$$\int_\Omega \left(\nabla\times \widetilde{E}_\rho^{(j)}\cdot\nabla\times W - k_0^2 n_\rho^2 \widetilde{E}_\rho^{(j)}\cdot W\right)dx = \\ -\int_{\mathcal{B}_\rho}(1-\gamma^2)k_0^2 n^2 e_j\cdot W\,dx - \int_{\mathcal{B}_\rho}(1-\gamma^2)k_0^2 n^2 E^{(j)}\cdot W\,dx \quad \forall\, W\in\mathcal{V}, \tag{7.6}$$

with $\widetilde{E}_\rho^{(j)} = E_\rho^{(j)} - E^{(j)}$. Let us consider a decomposition for $\widetilde{E}_\rho^{(j)}$ of the form

$$\widetilde{E}_\rho^{(j)} = P_\rho^{(j)} + Q_\rho^{(j)}. \tag{7.7}$$

Function $P_\rho^{(j)}\in\mathcal{V}$ is solution to

$$\int_\Omega \nabla\times P_\rho^{(j)}\cdot\nabla\times W\,dx = \int_{\mathcal{B}_\rho} A^{(j)}\cdot W\,dx \\ -\int_{\mathcal{B}_\rho}(1-\gamma^2)k_0^2 n^2 e_j\cdot W\,dx - \int_{\mathcal{B}_\rho}(1-\gamma^2)k_0^2 n^2 E^{(j)}\cdot W\,dx \quad \forall\, W\in\mathcal{V}, \tag{7.8}$$

where the constant vector $A^{(j)}\in\mathbb{C}^3$ has been introduced to fulfill the compatibility condition, namely

$$[A^{(j)}]_i = \frac{1}{|\mathcal{B}_\rho|}\int_{\mathcal{B}_\rho}(1-\gamma^2)k_0^2 n^2(\delta_{ij} + [E^{(j)}]_i)\,dx. \tag{7.9}$$

On the other hand, function $Q_\rho^{(j)}\in\mathcal{V}$ is solution to

$$\int_\Omega \left(\nabla\times Q_\rho^{(j)}\cdot\nabla\times W - k_0^2 n_\rho^2 Q_\rho^{(j)}\cdot W\right)dx = \int_\Omega k_0^2 n_\rho^2 P_\rho^{(j)}\cdot W\,dx \quad \forall\, W\in\mathcal{V}. \tag{7.10}$$

From the well-posedness of the above variational problem [48, 49], we have

$$\|Q_\rho^{(j)}\|_{\mathcal{V}} \le C\|P_\rho^{(j)}\|_{L^2(\Omega;\mathbb{C}^3)} \le C\|P_\rho^{(j)}\|_{\mathcal{V}}. \tag{7.11}$$

By setting $W = \overline{P}_\rho^{(j)}$ as test function in the variational problem (7.8), we obtain the equality

$$\int_\Omega \nabla\times P_\rho^{(j)}\cdot\nabla\times\overline{P}_\rho^{(j)}\,dx = \int_{\mathcal{B}_\rho} A^{(j)}\cdot\overline{P}_\rho^{(j)}\,dx - \int_{\mathcal{B}_\rho}(1-\gamma^2)k_0^2 n^2(e_j + E^{(j)})\cdot\overline{P}_\rho^{(j)}\,dx, \tag{7.12}$$

where $\overline{(\cdot)}$ is used to denote the complex conjugate of $(\cdot)$. From the Poincaré inequality [50], the above sesquilinear form is bounded from below as follows

$$C\|P_\rho^{(j)}\|_{\mathcal{V}}^2 \le \int_\Omega \nabla\times P_\rho^{(j)}\cdot\nabla\times\overline{P}_\rho^{(j)}\,dx. \tag{7.13}$$

By using the Cauchy-Schwarz inequality [51] and the Lebesgue differentiation theorem, we obtain the following upper bound

$$\int_\Omega \nabla\times P_\rho^{(j)}\cdot\nabla\times\overline{P}_\rho^{(j)}\,dx \le C\rho^{\frac{3}{2}}\|P_\rho^{(j)}\|_{L^2(\mathcal{B}_\rho;\mathbb{C}^3)}. \tag{7.14}$$

Notice that, Hölder inequality [51] and the Sobolev embedding theorem [52] can be used to derive

$$\|P_\rho^{(j)}\|_{L^2(\mathcal{B}_\rho;\mathbb{C}^3)} \leq C\rho^{\frac{3}{2q}}\|P_\rho^{(j)}\|_{L^{2p}(\mathcal{B}_\rho;\mathbb{C}^3)} \leq C\rho^{\delta}\|P_\rho^{(j)}\|_{H^1(\Omega;\mathbb{C}^3)}, \tag{7.15}$$

for any $1 < q < \infty$, with $1/p + 1/q = 1$, and $\delta = \frac{3}{2q}$. Therefore, by combining the above inequalities, we get

$$\|P_\rho^{(j)}\|_{\mathcal{V}} \leq C\rho^{\frac{3}{2}+\delta} \quad \text{and} \quad \|Q_\rho^{(j)}\|_{\mathcal{V}} \leq C\rho^{\frac{3}{2}+\delta}. \tag{7.16}$$

Finally, from the triangular inequality in (7.7) combined with the above estimates, we obtain the required result for any $0 < \delta < 3/2$, provided that $\|P_\rho^{(j)}\|_{H^1(\Omega;\mathbb{C}^3)} \leq C\|P_\rho^{(j)}\|_{\mathcal{V}}$. ☐

Remark 4. *The estimate* (7.4) *in Lemma 3 can be written simply as*

$$\|E_\rho^{(j)} - E^{(j)}\|_{\mathcal{V}} = o(\rho^{\frac{3}{2}}), \tag{7.17}$$

provided that $\delta > 0$. *The notation* $o(f(\rho))$ *has to be understood as*

$$\lim_{\rho\to 0}\frac{o(f(\rho))}{f(\rho)} = 0, \tag{7.18}$$

with $f(\rho)$ *used to denote a real-valued function that goes monotonically to zero when* $\rho \to 0$.

7.2. **Topological Asymptotic Expansion of the Effective Permittivity.** By using the definition for the contrast (2.6), we can rewrite the perturbed effective permittivity from (7.3) as follows

$$\begin{aligned}[\varepsilon_{\text{eff}}^{\rho}]_{ij} = &\frac{1}{|\Omega|}\int_\Omega n^2[E_\rho^{(j)}]_i\,dx + \frac{1}{|\Omega|}\int_\Omega n^2\delta_{ij}\,dx \\ &- \frac{1}{|\Omega|}\int_{\mathcal{B}_\rho(\widehat{x})}(1-\gamma^2)n^2\left(\delta_{ij} + [E_\rho^{(j)}]_i\right)dx,\end{aligned} \tag{7.19}$$

Now, we can evaluate the difference

$$\begin{aligned}[\varepsilon_{\text{eff}}^{\rho}]_{ij} - [\varepsilon_{\text{eff}}]_{ij} &= \frac{1}{|\Omega|}\int_\Omega n^2[\widetilde{E}_\rho^{(j)}]_i\,dx - \frac{1}{|\Omega|}\int_{\mathcal{B}_\rho(\widehat{x})}(1-\gamma^2)n^2\left(\delta_{ij} + [E_\rho^{(j)}]_i\right)dx \qquad (7.20)\\ &= \frac{1}{|\Omega|}\int_\Omega n^2[\widetilde{E}_\rho^{(j)}]_i\,dx - \frac{1}{|\Omega|}\int_{\mathcal{B}_\rho(\widehat{x})}(1-\gamma^2)n^2\left(\delta_{ij} + [E^{(j)}]_i\right)dx + \mathcal{E}_1(\rho),\end{aligned}$$

where $[\widetilde{E}_\rho^{(j)}]_i := [E_\rho^{(j)}]_i - [E^{(j)}]_i$ and $\mathcal{E}_1(\rho)$ is defined as

$$\begin{aligned}\mathcal{E}_1(\rho) &:= -\frac{1}{|\Omega|}\int_{\mathcal{B}_\rho(\widehat{x})}(1-\gamma^2)n^2[\widetilde{E}_\rho^{(j)}]_i\,dx, \\ |\mathcal{E}_1(\rho)| &\leq C\rho^{\frac{3}{2}}\|\widetilde{E}_\rho^{(j)}\|_{L^2(\mathcal{B}_\rho;\mathbb{C}^3)} \\ &\leq C\rho^{\frac{3}{2}}\|\widetilde{E}_\rho^{(j)}\|_{\mathcal{V}} = o(\rho^3),\end{aligned} \tag{7.21}$$

where we have used Lemma 3. The first integral from (7.20) can be replaced by

$$\frac{1}{|\Omega|}\int_\Omega n^2[\widetilde{E}_\rho^{(j)}]_i\,dx = \frac{1}{k_0^2|\Omega|}\int_\Omega k_0^2 n^2 e_i\cdot\widetilde{E}_\rho^{(j)}\,dx. \tag{7.22}$$

From the definition for the contrast (2.6), the perturbed counterpart of the j-th cell-problem (7.2) can be rewritten in the following convenient form

$$\begin{aligned}\int_\Omega\left(\nabla\times E_\rho^{(j)}\cdot\nabla\times W - k_0^2n^2\,E_\rho^{(j)}\cdot W\right)dx = \int_\Omega k_0^2n^2e_j\cdot W dx - \\ \int_{\mathcal{B}_\rho}(1-\gamma^2)k_0^2n^2e_j\cdot W\,dx - \int_{\mathcal{B}_\rho}(1-\gamma^2)k_0^2n^2E_\rho^{(j)}\cdot W\,dx.\end{aligned} \tag{7.23}$$

After subtracting (2.2) from the above equation, we obtain

$$\int_\Omega \left(\nabla\times \widetilde{E}^{(j)}_\rho\cdot\nabla\times W - k_0^2 n^2\,\widetilde{E}^{(j)}_\rho\cdot W\right)dx = \\ -\int_{\mathcal{B}_\rho}(1-\gamma^2)k_0^2n^2 e_j\cdot W\,dx - \int_{\mathcal{B}_\rho}(1-\gamma^2)k_0^2n^2 E^{(j)}_\rho\cdot W\,dx. \quad (7.24)$$

By setting $W = E^{(i)}$ as a test function in the above result and $W=\widetilde{E}^{(i)}_\rho$ as a test function in (2.2), we obtain the following important equality after comparing both resulting expressions

$$\int_\Omega k_0^2n^2 e_i\cdot\widetilde{E}^{(j)}_\rho dx = -\int_{\mathcal{B}_\rho}(1-\gamma^2)k_0^2n^2 e_j\cdot E^{(i)}\,dx \\ -\int_{\mathcal{B}_\rho}(1-\gamma^2)k_0^2n^2E^{(j)}\cdot E^{(i)}\,dx - \int_{\mathcal{B}_\rho}(1-\gamma^2)k_0^2n^2E^{(i)}\cdot\widetilde{E}^{(j)}_\rho\,dx, \quad (7.25)$$

where we have used the symmetry of the sesquilinear forms. Therefore, the difference (7.20) can be rewritten as

$$[\varepsilon^\rho_{\text{eff}}]_{ij} - [\varepsilon_{\text{eff}}]_{ij} = -\frac{1}{|\Omega|}\int_{\mathcal{B}_\rho(\widehat{x})}(1-\gamma^2)n^2(\delta_{ij}+[E^{(i)}]_j+[E^{(j)}]_i+E^{(i)}\cdot E^{(j)})dx + \mathcal{E}(\rho), \quad (7.26)$$

where $\mathcal{E}(\rho)=\mathcal{E}_1(\rho)+\mathcal{E}_2(\rho)$, with $\mathcal{E}_2(\rho)$ defined as

$$\begin{aligned}\mathcal{E}_2(\rho) &:= -\frac{1}{|\Omega|}\int_{\mathcal{B}_\rho(\widehat{x})}(1-\gamma^2)n^2E^{(i)}\cdot\widetilde{E}^{(j)}_\rho\,dx,\\ |\mathcal{E}_2(\rho)| &\le C\rho^{\frac{3}{2}}\|\widetilde{E}^{(j)}_\rho\|_{L^2(\mathcal{B}_\rho;\mathbb{C}^3)}\\ &\le C\rho^{\frac{3}{2}}\|\widetilde{E}^{(j)}_\rho\|_{\mathcal{V}} = o(\rho^3),\end{aligned} \quad (7.27)$$

where we have used Lemma 3. Finally, from the Lebesgue differentiation theorem, we obtain the following topological asymptotic expansion

$$[\varepsilon^\rho_{\text{eff}}]_{ij} = [\varepsilon_{\text{eff}}]_{ij} - \frac{4}{3}\pi\rho^3\frac{1-\gamma^2}{|\Omega|}n^2(\delta_{ij}+[\widehat{E}^{(i)}]_j+[\widehat{E}^{(j)}]_i+\widehat{E}^{(i)}\cdot\widehat{E}^{(j)})(\widehat{x}) + o(\rho^3), \quad (7.28)$$

which allows for identifying the topological derivative of the Cartesian components of the effective permittivity second-order tensor, namely

$$[D_T\varepsilon_{\text{eff}}]_{ij}(\widehat{x}) = -\frac{1-\gamma^2}{|\Omega|}n^2(\delta_{ij}+[\widehat{E}^{(i)}]_j+[\widehat{E}^{(j)}]_i+\widehat{E}^{(i)}\cdot\widehat{E}^{(j)})(\widehat{x}), \quad (7.29)$$

where $\widehat{(\cdot)}$ is used to represent a mean value of $(\cdot)$ around the point $\widehat{x}\in\Omega$.

ACKNOWLEDGEMENTS

This research was partly supported by CNPq (Brazilian Research Council), FAPERJ (Research Foundation of the State of Rio de Janeiro), and CAPES (Coordination for the Improvement of Higher Education Personnel). These financial supports are gratefully acknowledged. We also thank Dr. Lucas Heitzmann Gabrielli for the fruitful early discussions.

REFERENCES

[1] John D Joannopoulos, Steven G Johnson, Joshua N Winn, and Robert D Meade. Molding the flow of light. *Princet. Univ. Press. Princeton, NJ [ua]*, 12:33, 2008.

[2] Stefan A Maier et al. *Plasmonics: fundamentals and applications*, volume 1. Springer, 2007.

[3] Nader Engheta and Richard W Ziolkowski. *Metamaterials: physics and engineering explorations*. John Wiley & Sons, 2006.

[4] Nathaniel Kinsey, Clayton DeVault, Alexandra Boltasseva, and Vladimir M Shalaev. Near-zero-index materials for photonics. *Nature Reviews Materials*, 4(12):742–760, 2019.

[5] Iñigo Liberal and Nader Engheta. Near-zero refractive index photonics. *Nature Photonics*, 11(3):149–158, 2017.

[6] Michaël Lobet, Nathaniel Kinsey, Iñigo Liberal, Humeyra Caglayan, Paloma A Huidobro, Emanuele Galiffi, Jorge Ricardo Mejía-Salazar, Giovanna Palermo, Zubin Jacob, and Nicolò Maccaferri. New horizons in near-zero refractive index photonics and hyperbolic metamaterials. *ACS photonics*, 10(11):3805–3820, 2023.

[7] Daryl I Vulis, Orad Reshef, Philip Camayd-Muñoz, and Eric Mazur. Manipulating the flow of light using dirac-cone zero-index metamaterials. *Reports on Progress in Physics*, 82(1):012001, 2018.

[8] Inigo Liberal and Nader Engheta. The rise of near-zero-index technologies. *Science*, 358(6370):1540–1541, 2017.

[9] Mário Silveirinha and Nader Engheta. Tunneling of electromagnetic energy through subwavelength channels and bends using ε-near-zero materials. *Physical review letters*, 97(15):157403, 2006.

[10] Andrea Alu, Mário G Silveirinha, Alessandro Salandrino, and Nader Engheta. Epsilon-near-zero metamaterials and electromagnetic sources: Tailoring the radiation phase pattern. *Physical Review B—Condensed Matter and Materials Physics*, 75(15):155410, 2007.

[11] Jiaye Wu, Ze Tao Xie, Yanhua Sha, HY Fu, and Qian Li. Epsilon-near-zero photonics: infinite potentials. *Photonics Research*, 9(8):1616–1644, 2021.

[12] Junho Yoon, Ming Zhou, Md Alamgir Badsha, Tae Young Kim, Young Chul Jun, and Chang Kwon Hwangbo. Broadband epsilon-near-zero perfect absorption in the near-infrared. *Scientific reports*, 5(1):12788, 2015.

[13] M Zahirul Alam, Israel De Leon, and Robert W Boyd. Large optical nonlinearity of indium tin oxide in its epsilon-near-zero region. *Science*, 352(6287):795–797, 2016.

[14] Orad Reshef, Israel De Leon, M Zahirul Alam, and Robert W Boyd. Nonlinear optical effects in epsilon-near-zero media. *Nature Reviews Materials*, 4(8):535–551, 2019.

[15] Luca Dal Negro and Marco Ornigotti. Nonlinear quantum electrodynamics of epsilon-near-zero media. *arXiv e-prints*, pages arXiv–2412, 2024.

[16] Xinxiang Niu, Xiaoyong Hu, Saisai Chu, and Qihuang Gong. Epsilon-near-zero photonics: a new platform for integrated devices. *Advanced Optical Materials*, 6(10):1701292, 2018.

[17] Hao Li, Ziheng Zhou, Yijing He, Wangyu Sun, Yue Li, Iñigo Liberal, and Nader Engheta. Geometry-independent antenna based on epsilon-near-zero medium. *Nature communications*, 13(1):3568, 2022.

[18] Wenhe Jia, Meng Liu, Yongchang Lu, Xi Feng, Qingwei Wang, Xueqian Zhang, Yibo Ni, Futai Hu, Mali Gong, Xinlong Xu, et al. Broadband terahertz wave generation from an epsilon-near-zero material. *Light: Science & Applications*, 10(1):11, 2021.

[19] Hongchen Chu, Qi Li, Bingbing Liu, Jie Luo, Shulin Sun, Zhi Hong Hang, Lei Zhou, and Yun Lai. A hybrid invisibility cloak based on integration of transparent metasurfaces and zero-index materials. *Light: Science & Applications*, 7(1):50, 2018.

[20] Yasaman Kiasat, Maria Grazia Donato, Michael Hinczewski, Mohamed ElKabbash, Theodore Letsou, Rosalba Saija, Onofrio Maria Maragò, Giuseppe Strangi, and Nader Engheta. Epsilon-near-zero (enz)-based optomechanics. *Communications Physics*, 6(1):69, 2023.

[21] Hamid Reza Darabian, Johann Toudert, Konstantin Y Bliokh, and Dorota Anna Pawlak. Compendium of natural epsilon-near-zero materials. *ACS Photonics*, 2025.

[22] Ward D Newman, Cristian L Cortes, Jon Atkinson, Sandipan Pramanik, Raymond G DeCorby, and Zubin Jacob. Ferrell–berreman modes in plasmonic epsilon-near-zero media. *Acs Photonics*, 2(1):2–7, 2015.

[23] Maxim A Gorlach and Mikhail Lapine. Boundary conditions for the effective-medium description of subwavelength multilayered structures. *Physical Review B*, 101(7):075127, 2020.

[24] Mohsin Habib, Daria Briukhanova, Nekhel Das, Bilge Can Yildiz, and Humeyra Caglayan. Controlling the plasmon resonance via epsilon-near-zero multilayer metamaterials. *Nanophotonics*, 9(11):3637–3644, 2020.

[25] Saman Jahani and Zubin Jacob. All-dielectric metamaterials. *Nature nanotechnology*, 11(1):23–36, 2016.

[26] Yeon Ui Lee, Eleonora Garoni, Hanayo Kita, Kenji Kamada, Byung Hoon Woo, Young Chul Jun, Sang Min Chae, Hyo Jung Kim, Kwang Jin Lee, Seokhyun Yoon, et al. Strong nonlinear optical response in the visible spectral range with epsilon-near-zero organic thin films. *Advanced Optical Materials*, 6(14):1701400, 2018.

[27] M. P. Bendsøe and O. Sigmund. *Topology optimization. Theory, methods and applications.* Springer-Verlag, Berlin, 2003.

[28] S. Osher and R. Fedkiw. *Level set methods and dynamic implicit surfaces.* Springer-Verlag, New York, 2003.

[29] N. Provatas and K. Elder. *Phase-Field Methods in Materials Science and Engineering.* Wiley-VCH, 2010.

[30] A.A. Novotny and J. Sokołowski. *Topological derivatives in shape optimization.* Interaction of Mechanics and Mathematics. Springer-Verlag, Berlin, Heidelberg, 2013.

[31] S. Amstutz, S.M. Giusti, A.A. Novotny, and E.A. de Souza Neto. Topological derivative for multi-scale linear elasticity models applied to the synthesis of microstructures. *International Journal for Numerical Methods in Engineering*, 84:733–756, 2010.

[32] V. Calisti, A. Lebée, A.A. Novotny, and J. Sokolowski. Emergence of elastostatic strain-gradient effects from topological optimization. *European Journal of Mechanics, A/Solids*, 100:104979, 2023.

[33] C.G. Méndez, J.M. Podestá, O. Lloberas-Valls, S. Toro, A.E. Huespe, and J. Oliver. Computational material design for acoustic cloaking. *International Journal for Numerical Methods in Engineering*, 112(10):1353–1380, 2017.

[34] J.M. Podestá, C.M. Méndez, S. Toro, and A.E. Huespe. Symmetry considerations for topology design in the elastic inverse homogenization problem. *Journal of the Mechanics and Physics of Solids*, 128:54–78, 2019.

[35] N. Rossi, J.M. Podestá, F. Bre, C.G. Méndez, and A.E. Huespe. A microarchitecture design methodology to achieve extreme isotropic elastic properties of composites based on crystal symmetries. *Structural and Multidisciplinary Optimization*, 63:2459–2472, 2021.

[36] R. Yera, N. Rossi, C.G. Méndez, and A.E. Huespe. Topology design of 2d and 3d elastic material microarchitectures with crystal symmetries displaying isotropic properties close to their theoretical limits. *Applied Material Today*, 18:100456, 2020.

[37] P.J. Blanco, F.A. Pinheiro, and A.A. Novotny. A novel multiscale model for microstructured electromagnetic media. *Proceedings of the Royal Society A: Mathematical, Physical and Engineering Sciences*, 4802:0240495, 2024.

[38] S. Garreau, Ph. Guillaume, and M. Masmoudi. The topological asymptotic for PDE systems: the elasticity case. *SIAM Journal on Control and Optimization*, 39(6):1756–1778, 2001.

[39] J. Sokołowski and A. Żochowski. On the topological derivative in shape optimization. *SIAM Journal on Control and Optimization*, 37(4):1251–1272, 1999.

[40] A.A. Novotny, S.M. Giusti, and S. Amstutz. Guest Editorial: On the topological derivative method and its applications in computational engineering. *Engineering Computations*, 39(1):1–2, 2022.

[41] S. Amstutz and H. Andrä. A new algorithm for topology optimization using a level-set method. *Journal of Computational Physics*, 216(2):573–588, 2006.

[42] S. Amstutz. Analysis of a level set method for topology optimization. *Optimization Methods and Software*, 26(4-5):555–573, 2011.

[43] C. Chen, Z. Wang, K. Wu, and H. Ye. Tunable near-infrared epsilon-near-zero and plasmonic properties of Ag-ITO co-sputtered composite films. *Science and Technology of Advanced Materials*, 19(1):174–184, 2018.

[44] P.B. Johnson and R.W. Christy. Optical constants of the noble metals. *Physical Review B*, 6(12):4370, 1972.

[45] J.C. Nédélec. Mixed finite elements in $\mathbb{R}^3$. *Numerische Mathematik*, 35:315–341, 1980.

[46] Frédéric Hecht. FreeFEM documentation. 2022. `https://doc.freefem.org/introduction/index.html#` (Accessed in August 2022).

[47] Ari H Sihvola. *Electromagnetic mixing formulas and applications.* Number 47. Iet, 1999.

[48] A. Bossavit. *Computational Electromagnetism.* Electromagnetism. Academic Press, San Diego, 1998.

[49] P. Monk. *Finite Element Methods for Maxwell's Equations.* Numerical Mathematics and Scientific Computation. Oxford University Press, Oxford, UK, 2003.

[50] D. Pauly and J. Valdman. Poincaré–Friedrichs type constants for operators involving grad, curl, and div: Theory and numerical experiments. *Computers & Mathematics with Applications*, 79(11):3027–3067, 2020.

[51] A. Quarteroni and A. Valli. *Numerical Approximation of Partial Differential Equations.* Springer-Verlag, Berlin, Heidelberg, 1997.

[52] R. Dautray and J. L. Lions. *Mathematical analysis and numerical methods for science and technology. Volume 2 – Functional and Variational Methods.* Springer-Verlag, Berlin, Heidelberg, New York, 1988.

(A.A. Novotny and P.J. Blanco) Laboratório Nacional de Computação Científica LNCC/MCTI, Coordenação de Métodos Matemáticos e Computacionais, Av. Getúlio Vargas 333, 25651-075 Petrópolis - RJ, Brasil

Email address: `{novotny,pjblanco}@lncc.br`

(F.A. Pinheiro) Instituto de Física, Universidade Federal do Rio de Janeiro, Caixa Postal 68528, Rio de Janeiro, Rio de Janeiro 21941-972, Brazil

Email address: `fpinheiro@if.ufrj.br`